Enhanced iceberg discharge in the western North Atlantic during all Heinrich events of the last glaciation

Yuxin Zhou[1,2], Jerry F. McManus[1,2], Allison W. Jacobel[3,4], Kassandra M. Costa[5], Shouyi Wang[5], Blanca Alvarez Caraveo[6]

[1]Lamont-Doherty Earth Observatory of Columbia University, Palisades, NY 10964, USA

[2]Dept. of Earth and Environmental Sciences, Columbia University, New York, NY 10027, USA

[3]Institute at Brown for Environment and Society, Providence, RI 02912, USA

[4]Dept. of Earth, Environmental, and Planetary Sciences, Brown University, Providence, RI 02912, USA

[5]Dept. of Geology and Geophysics, Woods Hole Oceanographic Institution, Woods Hole, MA 02543, USA

[6]Dept. of Atmospheric and Oceanic Sciences, University of California, Los Angeles, Los Angeles, CA 90095, USA

Correspondence:

Yuxin Zhou

yzhou@ldeo.columbia.edu

Abstract

A series of catastrophic iceberg discharges to the North Atlantic, termed Heinrich events, punctuated the last ice age. During Heinrich events, coarse terrigenous debris released from the drifting icebergs was preserved in deep-sea sediments, serving as an indicator of iceberg passage. Quantifying the vertical flux of ice-rafted debris (IRD) in open-ocean settings can resolve questions regarding the timing and spatial variation in ice sheet calving intensity. In this study, $^{230}Th_{xs}$-based IRD flux throughout the last glacial period was measured in a deep-sea sediment core from the western North Atlantic, and complemented by data spanning 0-32 ka from a sediment core in the Labrador Sea. The cores were recovered from sites downstream from Hudson Strait, a likely conduit for icebergs calving from the Laurentide ice sheet (LIS). We compare our results with equivalent existing data from the eastern North Atlantic and show that the two cores in our study have higher IRD fluxes during all Heinrich events, notably including events H3 (~31 ka) and H6 (~60 ka). This study demonstrates that the LIS played a role in all Heinrich events, and raises the likelihood that a single mechanism can account for the genesis of these events.

Keywords: Heinrich event; western North Atlantic; IRD flux; thorium normalization

1. Introduction

The last glaciation was characterized by two types of millennial-scale climate change. The classic Greenland ice core records document Dansgaard-Oeschger (D-O) events, rapid shifts in air temperature over the ice cap of ~8 °C within a few decades (Dansgaard et al., 1993; Grootes et al., 1993; Johnsen et al., 1992; NGRIP members, 2004). Throughout the same interval, subpolar North Atlantic deep-sea sediments preserve evidence of century-scale episodes of catastrophic iceberg discharge known as Heinrich events (HEs). The passage of icebergs is marked by ice-rafted debris (IRD), which forms layers of detrital material in glacial sediment sequences (Bond et al., 1992; Broecker et al., 1992; Heinrich, 1988; Hemming, 2004).

The icebergs discharged during HEs drifted and melted across the subpolar North Atlantic Ocean, an important region of deep-water formation that is sensitive to disruption by surface water freshening (Manabe and Stouffer, 1997; Rahmstorf, 1995). Indeed, the freshwater flux associated with these events is thought to have dramatically and repeatedly weakened the Atlantic Meridional Overturning Circulation (AMOC) (Henry et al., 2016; McManus et al., 2004). As a result, the Northern Hemisphere cooled (Bard et al., 2000; Bond et al., 1993) while the Southern Hemisphere warmed (Barker et al., 2009; Buizert et al., 2018). The oceans, cryosphere, and atmosphere all respond in connected ways during HEs, making these events ideal targets for examining how abrupt climate change unfolds.

An unsolved mystery of HEs is the apparently anomalous behavior associated with H3 (~31 ka) and H6 (~60 ka). These two events are often regarded as atypical because of their relatively low IRD concentrations and the absence of detrital carbonates in the eastern subpolar North Atlantic (Broecker et al., 1992). In this paper, we will refer to the other HEs, H1, H2, H4, and H5, as the "typical" HEs and H3 and H6 as "atypical". The observed differences between the typical and the atypical events have been explained by the variable behavior of the ocean or the cryosphere. The robustness of these divergent observations is relevant to understanding the mechanism(s) accounting for these dramatic events. Similar behavior of the events would fit more readily into a single mechanism, while contrasting behavior suggests different, even drastically divergent, mechanisms or causes at different times. From a glaciological perspective, the provenance of IRD in H3 and H6 suggests a European ice sheet origin that led to smaller iceberg fluxes in the western North Atlantic (Grousset et al., 2000, 1993; Peck et al., 2007; Snoeckx et al., 1999), although this claim has been disputed (Jullien et al., 2006). A complementary hypothesis suggests that H3 and H6 occurred at the onset of Marine Isotope Stage (MIS) 2 and MIS4 when the LIS was just starting to grow, resulting in a smaller magnitude of calving (Gwiazda et al., 1996). From an oceanographic perspective, assuming that all the events originated from the LIS, warmer sea-surface temperatures might have melted the icebergs closer to their western source during the two atypical HEs (Bond et al., 1992). Consistent with that view, Pb isotope data suggest that, in the eastern North Atlantic, the relatively IRD-rich layers are actually the results of foraminifera-dissolution events (Gwiazda et al., 1996). The lack of foraminifera in these layers would cause an apparent increase in the proportion of IRD, the other major coarse constituent in North Atlantic sediments.

Reconstructing the IRD deposition rate provides a straightforward test of these competing hypotheses. If the increased IRD concentrations in H3 and H6 are solely the result of foraminifera dissolution, the IRD fluxes (deposition rate per unit area per unit time) during these periods should not increase. If the icebergs originated and mostly melted in the west during the atypical HEs, the IRD fluxes would have been higher in the west than the east. The atypical HE IRD fluxes might also have been even higher than during the typical HEs at the western sites, assuming the total magnitude of calving remained the same. If the Laurentide ice sheet calving increased by a limited amount during the atypical HEs, the IRD fluxes would have shown a visible but smaller increase than the typical HEs throughout the basin. Lastly, if the two events did originate from the European ice sheet, the IRD fluxes in the east should have been higher than the west.

Resolving IRD fluxes during HEs provides a way to test the aforementioned hypotheses regarding the two atypical events. This hypothesis-testing can be achieved with ^{230}Th normalization. The rapid scavenging of ^{230}Th results in a near balance between its burial and local production, allowing it to be used to reconstruct vertical mass flux (Bacon, 1984; Bacon and Anderson, 1982; Bacon and Rosholt, 1982; Costa et al., 2020; Francois et al., 2004). IRD flux can therefore be reconstructed from the ^{230}Th-normalized burial flux of sediment that is uniquely identified as IRD.

Previously, century-scale measurements of IRD have only been made in the eastern North Atlantic (McManus et al., 1998). Here we present a 135-thousand-year (kyr) ice-rafting record off the coast of Newfoundland, 2200 km downstream from the Hudson Strait. We complement it with a record from Orphan Knoll that is ~1700 km downstream from the Hudson Strait and extends through H3. By comparing our ice-rafting records with the directly equivalent existing data in the eastern North Atlantic (McManus et al., 1998), we demonstrate that H3 and H6 are mechanistically consistent with the other HEs of the last glaciation.

2. Methods

EW9303-37JPC (43.68°N, 46.28°W, 3981m, IGSN: DSR000507, JPC37 hereafter) is a 13.315-m-long jumbo piston core retrieved at the foot of a continental slope off the coast of Newfoundland, Canada (Figure 1). DY081-GVY001 (50°09’36’’N, 45°30’36’’W, 3721m, GVY001 hereafter) is a gravity core retrieved near Orphan Knoll (Figure 1, Hendry et al. 2019). Both sites are presently under the influence of the surficial Labrador Current, which transports icebergs southward in the

Labrador Sea. At depth, the deep western boundary current (DWBC) also flows southward past the sites (McCartney, 1992).

Samples of 8-10 g were taken at 2 cm intervals from JPC37, and at 5 cm intervals from GVY001, then freeze dried, weighed, and washed through 63 μm sieves to separate coarse and fine fractions. The proportion of coarse sediment (% coarse) was calculated by dividing the dried >63 μm fraction weight by the total dry weight. Subsequently, the coarse fraction was dry-sieved at >150 μm and split so that 300-400 foraminifera shells and ~100 IRD grains could be identified and counted under a microscope. Foraminifera counts were used to calculate the relative abundance of the polar planktic foraminifera, *Neogloboquadrina pachyderma* (hereafter *N. pachy.*), calculated as the number of *N. pachy.* specimens in a sample divided by the total number of planktic foraminifera shells. The relative abundance of IRD (hereafter % IRD) was calculated as the number of IRD grains divided by the sum of IRD grains plus planktic foraminifera shells.

During microscope counting work, eight to ten specimens of *N. pachy.* were picked for $\delta^{18}O$ and $\delta^{13}C$ analysis in the Lamont-Doherty Earth Observatory of Columbia University (LDEO) stable isotope laboratory, using a Thermo Delta V Plus equipped with a Kiel IV individual acid-bath sample preparation device. Measurements made on standard carbonate NBS19 yield a standard deviation of 0.06% for $\delta^{18}O$ and 0.03% for $\delta^{13}C$.

Elemental intensities from JPC37 were measured using an X-ray fluorescence (XRF) core scanner (ITRAX, Cox Ltd., Sweden) at LDEO at 2mm resolution, using an integration time of 10s and a molybdenum x-ray source set to 30 kV and 50 mA. The intensities were calibrated with flux fusion concentration measurements from JPC37, following the procedure of Murray et al. (2000). Sediment samples spanning the range of XRF intensities were randomized, interspersed with standard reference materials (e.g., JLS-1, JDO-1, SCO-1, AGV-2, DTS-2b, W-2a), ashed, digested in HF and HNO_3 overnight, and diluted for analysis on an Agilent 720 Inductively Coupled Plasma Optical Emission Spectrometer (ICP-OES) at LDEO. The ICP-OES data provide a robust calibration (R^2=0.80 for Ca, R^2=0.90 for Sr) for the high-resolution XRF records. Elemental intensities from GVY001 were measured from a similar ITRAX XRF core scanner at the British Ocean Sediment Core Research Facility (BOSCORF; Hendry et al. 2019). The elemental intensities from GVY001 are uncalibrated and presented as ratios.

Bulk wet density and magnetic susceptibility from JPC37 were obtained at 1cm resolution from a Geotek multi-sensor core logger at the Lamont-Doherty Core Repository. Local anomalously low-density peaks were identified as cracks formed due to drying and omitted in data processing. Bulk wet density and magnetic susceptibility from GVY001 were obtained at 1cm resolution from a similar Geotek instrument at BOSCORF.

Each bulk sediment sample of ~100 mg was spiked, digested (Fleisher and Anderson, 1991), purified (Lao et al., 1993), and analyzed for uranium and thorium isotope activities. The last step was done on an Element Plus inductively coupled plasma mass spectrometer (ICP-MS) at LDEO. The conversion from raw counting data to activities and associated error propagation has been packaged into a Python script named ThxsPy accessible at https://github.com/yz3062/ThxsPy.

Sediment fluxes were calculated using $^{230}Th_{xs}$, which is the ^{230}Th derived from the decay of ^{234}U in seawater and subsequently scavenged by adsorption onto settling particles. To calculate ^{230}Thxs, other sources of non-excess ^{230}Th need to be quantified and removed (Bacon, 1984; Costa and McManus, 2017; Francois et al., 2004, 1990).

First, detrital ^{230}Th is the ^{230}Th produced from the radioactive decay of ^{238}U in mineral lattices. Detrital ^{238}U can be estimated by assuming a constant detrital ^{238}U/^{232}Th and that all measured

^{232}Th is detrital. A range of $(^{238}U/^{232}Th)_{detrital}$ between 0.47 and 0.7 has been used by previous studies in this region (Table 1). We conducted a leaching experiment in JPC37 to isolate the detrital uranium and thorium and determined $(^{238}U/^{232}Th)_{detrital}$ to be 0.48. We further determined from the leaching experiment the disequilibrium in $(^{230}Th/^{238}U)_{detrital}$ caused by α recoil to be 0.81 (details in Discussion).

Next, ^{230}Th can also be produced from the radioactive decay of ^{238}U that precipitated from the soluble form U(VI) to its insoluble form U(IV) in anoxic, reducing sediments (Barnes and Cochran, 1990; Klinkhammer and Palmer, 1991). Assuming the non-detrital portion of ^{238}U is authigenic, the derived ^{230}Th (abbreviated to authigenic ^{230}Th) can be calculated using a seawater $^{234}U/^{238}U$ of 1.1468 (Andersen et al., 2010) and applying the classic radio-decay equations.

In summary, the calculation of $^{230}Th_{xs}$ is thus

$$^{230}Th_{xs} = {}^{230}Th_{measured} - {}^{230}Th_{detrital} - {}^{230}Th_{authigenic}$$

$$= {}^{230}Th_{measured} - (^{238}U/^{232}Th)_{detrital} * (^{230}Th/^{238}U)_{detrital} * {}^{232}Th_{measured} - (^{238}U_{measured} - (^{238}U/^{232}Th)_{detrital} * (^{230}Th/^{238}U)_{detrital} * {}^{232}Th_{measured}) * [(1-e^{-\lambda 230*t}) + \lambda_{230}/(\lambda_{230}-\lambda_{234})(e^{-\lambda 234*t} - e^{-\lambda 230*t})((^{234}U/^{238}U)_{seawater}-1)]$$

Where $(^{238}U/^{232}Th)_{detrital}$ is 0.48, $(^{230}Th/^{238}U)_{detrital}$ is 0.81, λ is the isotope decay constant, $(^{234}U/^{238}U)_{seawater}$ is 1.1468, and t is the time of decay since deposition.

The values of $(^{238}U/^{232}Th)_{detrital}$ and $(^{230}Th/^{238}U)_{detrital}$ used by this study are different from most previous studies and are based on experimental results. We conducted leaching experiments throughout core JPC37 to obtain representative lattice-bound isotopic ratios. Bulk samples were leached with 5mL of 1N or 3N HCl and sonicated for 20 minutes. After a 5-minute centrifuge, the supernatant was decanted. In some cases, the supernatant was filtered using 0.42 μm filters. The rest of the procedure is the same as described above for typical sediment U-Th analysis. The strength of acid and time of sonication used were shown previously to remove authigenic uranium effectively without leaching lattice-bound uranium and thorium (Robinson et al., 2008).

From $^{230}Th_{xs}$, we can calculate the vertical mass flux

$$F = \beta * Z / {}^{230}Th_{xs,0}$$

Where F is the vertical mass flux, β is the production rate of ^{230}Th, Z is the water depth, and $^{230}Th_{xs,0}$ is $^{230}Th_{xs}$ corrected for decay since deposition using the independent age model. Everywhere else in this paper, we use $^{230}Th_{xs}$ as a shorthand of $^{230}Th_{xs,0}$. We can further calculate the IRD flux

$$\text{IRD flux} = F * \#\text{IRD} / M$$

where #IRD is the total number of IRD grains, and M is the dry bulk mass.

Cross correlation was performed on the time series of $\delta^{18}O$ of *N. pachy.* and $^{230}Th_{xs}$ to identify any lead or lag between the two. The 65-10 ka portions of both proxies were first extrapolated to a common time step of 500 years. The pairwise correlation was then computed for the two time series, first on their original chronology, then by offsetting the two by both positive and negative time steps. In each direction, up to 15 steps of offset were tested and the correlation coefficient calculated in each. The cross correlation was then bootstrapped 1000 times, allowing sampling interval and time step to vary.

3. Chronology

The chronology of JPC37 from modern to ~46 ka is based on radiocarbon dating. A monospecific sample of 350-400 specimens of *N. pachy.*, the most abundant foraminifera species in this core, were picked from the >150μm fraction. These foraminifera shells were sonicated in water and ethanol to remove any fine-grained sediment, including detrital carbonate that can potentially bias the results. Radiocarbon analyses were performed at NOSAMS-WHOI facility (see Appendix A for a link to data). The calibration to calendar ages uses Marine 13 and the CALIB program (Stuiver et al., 2019). We used 400 years as the marine reservoir correction (Reimer et al., 2013).

The chronology beyond the range of radiocarbon is determined by aligning our % *N. pachy*. with an alkenone-based sea-surface temperatures (SST) record from MD01-2444 (Martrat et al., 2007). The polar foraminifera *N. pachy.* lives in the coldest environment among planktic species and its abundance in JPC37 signals low SST (Ericson, 1959). MD01-2444 (37°33.68′N, 10°08.53′W, 2637 m) is on the Iberian margin and its latitude is comparable to JPC37. Its chronology is based on temperature alignment with the North Greenland Ice Sheet Project (NGRIP) ice core during the last glacial (Anderson et al., 2006; Johnsen et al., 2001; NGRIP members, 2004; Rasmussen et al., 2006) and before that, Antarctica Dome C (EPICA Community Members, 2004; Parrenin et al., 2004). Even though the two sites sit on the opposite side of the North Atlantic basin, the prevailing westerlies and the resulting current put MD01-2444 downstream from JPC37. As a result, the temperatures at the two sites should be closely correlated during regional-scale climate changes. The advantage of aligning with this SST record instead of directly with NGRIP is twofold. First, both records reconstruct SST so the correlation does not need to consider meridional or air-sea signal propagation. Second, NGRIP stops at MIS 5e, whereas the SST records extend beyond that, allowing us to align the late MIS 6 segment of our core as well.

The core chronology is corroborated with tephrochronology. We found several concentrated zones of plates of glassy, bubble-wall shards, consistent with the description of Ruddiman and Glover (1972). The shards are mostly non-existent outside of the zones. The youngest of these zones, at 70 cm, is identified Ash Zone 1. The commonly assumed age of Ash Zone 1 (12.2 cal ka BP)

(Andrews and Voelker, 2018) is only 700 years apart from the radiocarbon-based age model. Ash Zone 2 is identified at 628.5 cm and was previously dated to 55.4 ka in the NGRIP record based on the GICC05 age model (Svensson et al., 2008) and 54.5 ka by Ar-Ar dating of the volcanic ash (Southon, 2004), whereas in our age model it is at 57.4 ka. Outside of these two zones, glass shard counts are also high at H3 and H6. We cannot rule out that the shards at Heinrich layer 3 were delivered by a gravity flow.

The chronology of GVY001 is based on radiocarbon and tephrochronology. Radiocarbon analysis (n=7) in this core follows the same procedure as in JPC37, except for the youngest sample at the depth of 2 cm. At that depth we used *G. bulloides* instead of *N. pachy.* since not enough *N. pachy.* were found. Although age offsets have been identified in co-occurring planktic species (Ausín et al., 2019; Brocker et al., 1988; Costa et al., 2017), our age model is not likely to be sensitive to offsets of centuries or even millennia at this one horizon. Ash Zone 1 is identified at 58 cm, and we use 12.2 ka BP as its age (Andrews and Voelker, 2018).

4. Results

The age models indicate moderately high sedimentation rates in both cores: ~10 cm/kyr in JPC37 and ~12 cm/kyr in GVY001 (Figure 2 and Figure S1). Core JPC37 captured the whole last glacial-interglacial cycle (MIS 1-5) and the very end of MIS 6, whereas core GVY001 extends to just beyond 30 ka. Crossed beddings of foraminifera-rich sands are found in JPC37 around depths 288 cm – near the depth where H3 is found – (Figure S2) and 1312 cm. These sands are likely caused by turbidites and could influence the interpretation of results from this particular interval. Data from H3 in JPC37 is therefore considered tentatively except for when it is supported by independent evidence from GVY001, which is from a different location not influenced by any turbidite deposits. GVY001 has a similarly high sedimentation rate as JPC37.

In JPC37, % IRD varies between 0% and 100% (Figure 3e). At five depths, % IRD reached 100%. At three other depths, % IRD reached 50%. The majority of the % IRD peaks are found in the upper (glacial) part of the core. Heinrich layers are identified by peaks in % IRD, as well as peaks of Ca/Sr that are indicative of detrital carbonate (Hodell et al., 2008), magnetic susceptibility, density, and % coarse (Figure 3). Layers with prominent increases in all of these proxies are present in MIS 2-4 and late MIS 6. H4 and H5 show the strongest signals in all of these proxies, consistent with previous findings (Hemming et al., 2004). Several episodes of smaller magnitude can be found during early MIS 5. The strongest peak of Ca/Sr appears at 1220 cm depth and is matched with a $^{230}Th_{xs}$ low. However, no signals in magnetic susceptibility, % coarse, % IRD, % *N. pachy*., or $\delta^{18}O$ are present at this depth (density data does not extend to this depth). This discrepancy suggests the delivery of fine detrital carbonates at a high rate without freshwater flux or lower SST. A possible explanation is a gravity flow that originates from a region with high concentration of detrital carbonates. In GVY001, % IRD ranges between 0% and 100% (Figure 3e). Compared to JPC37, % IRD in GVY001 is higher on average. Ca/Sr, magnetic susceptibility, density, and % coarse help identify HEs. Possibly due to GVY001's more poleward location and setting within the cold Labrador current, % IRD and % *N. pachy*. are saturated to 100% during most of the last glacial period.

In JPC37, % *N. pachy*. has a range between 1% and 99% (Figure 3f). Peaks of % *N. pachy*. can be found at the same or slightly above the depths of % IRD peaks. $\delta^{18}O$ of *N. pachy.* ranges between 1.2‰ and 4.1‰ and displays a hybrid signal that combines the typical sawtooth glacial-interglacial pattern and episodes of depletion corresponding to HEs. In each of the identified HEs, % *N. pachy*. increased while the $\delta^{18}O$ of *N. pachy.* decreased. During HEs, % *N. pachy*. continues to vary even when % IRD stabilizes at a high value.

Our leaching experiment on JPC37 sediments suggests that the recoil-related losses of ^{234}U and ^{230}Th are about 10% each on average in Heinrich layer detrital sediments and higher in between (Figure S3). The variations in $^{234}U/^{238}U$ are smaller than those of $^{230}Th/^{234}U$. We use 0.9 for $^{230}Th/^{234}U$ and $^{234}U/^{238}U$ and 0.81 for $^{230}Th/^{238}U$ for both cores. The leaching experiment also suggests a potentially broad range in the detrital $^{238}U/^{232}Th$ ratio (Figure S4), but the five leaching experiments made in Heinrich layer 4 have an average of 0.48, which we use in this study.

The $^{230}Th_{xs}$ profile from JPC37 contains values that vary between 0-5 dpm/g. Low $^{230}Th_{xs}$ values (<0.5 dpm/g) are observed at 16.3, 24.0, 38.1, 45.8, 60.6, 67.8 ka during the last glacial period. The low $^{230}Th_{xs}$ episodes have ages one thousand years within the previously determined HE ages (Hemming, 2004), which is broadly within the uncertainty of radiocarbon dating. One sample in H4 and another in late MIS 6 have $^{230}Th_{xs}$ so low that their 95% uncertainty range barely reach above 0. GVY001 resembles JPC37 in $^{230}Th_{xs}$ for the most part, except the periods before and after H2.

In JPC37, mass flux has a range between 2 g/cm^{2}kyr and 133 g/cm^{2}kyr, although higher mass fluxes are associated with higher uncertainties. There are nine peaks of mass flux. Outside of the mass flux peaks, mass flux fluctuates around 4 g/cm^{2}kyr. IRD flux varies between 1 grain/cm^{2}kyr and 560,000 grains/cm^{2}kyr. At eight depth ranges, the values of IRD flux reach above 50,000 grains/cm^{2}kyr. These depths coincide with HEs. The IRD fluxes during H5 and H11 are the highest among HEs, with values at or above 500,000 grains/cm^{2}kyr. The IRD fluxes during H2 and H4 are around 250,000 grains/cm^{2}kyr. The IRD fluxes at H1, H6, and the event prior to H6 are lower at 100,000 grains/cm^{2}kyr, 41,000 grains/cm^{2}kyr, and 42,000 grains/cm^{2}kyr, respectively. The IRD fluxes during each HE and the event prior to H6 are statistically distinct from the ambient IRD flux, even at the smallest event (H6), where the p-value of the “Student’s” t-Test is 4×10^{-6}. In

GVY001, mass flux ranges from 3 g/cm^{2}kyr to 40 g/cm^{2}kyr. The peaks of mass flux at GVY001 are lower than the peaks of JPC37, while the mass flux between the peak values clusters around 7 g/cm^{2}kyr. During H1-3, the mass fluxes are around 20-30 g/cm^{2}kyr. However, unlike JPC37, GVY001 shows a clearer signal of mass flux increase during Younger Dryas. The IRD flux from GVY001 ranges between 0 grains/cm^{2}kyr and 190,000 grains/cm^{2}kyr. It is the highest during H1 and H2 at or above 160,000 grains/cm^{2}kyr, followed by the Last Glacial Maximum at 120,000 grains/cm^{2}kyr, and H3 at 90,000 grains/cm^{2}kyr. A "Student's" t-Test shows that the H3 IRD flux is distinctly different from the ambient sediment (p-value=1×10^{-10}).

5. **Discussion**

5.1. Interpretation of IRD flux

HE sedimentary layers have been viewed as the possible result of intervals of decreased foraminifera productivity, foraminifera dissolution, increased IRD deposition, or some combination of those influences. Previously, the only $^{230}Th_{xs}$-based quantification of the depositional flux of grains that are uniquely identified as IRD during the HEs is from V28-82 in the eastern subpolar North Atlantic (McManus et al., 1998). The data from V28-82 showed that H1, H2, H4, and H5 were at least in part increased ice-rafting events, but left open the question for the two atypical events. Our new results from JPC37 and GVY001 reaffirm McManus et al.'s conclusion, showing increased IRD flux for the four most typical HEs (Figure 4 c). Additionally, here we show for the first time that, at least in the western North Atlantic, the sediment layers associated with H3 and H6 were also the result of increased ice-rafted deposition, rather than solely the result of reduced productivity near the sea surface or enhanced foraminifera dissolution on the seafloor.

IRD fluxes in V28-82 are approximately half of those in the IRD flux of the western cores during H1 and H2, and about half of the IRD flux of JPC37 during H4 and H5. Even larger differences between IRD fluxes in the east and west are observed during H3, H6, and H11. The increases in IRD fluxes in V28-82 are muted during these events, whereas the IRD flux from JPC37 during H3 is thirty times higher than V28-82, during H6 nine times higher, and during H11 twenty times higher. Although H3 in JPC37 is near what may be a turbidite deposit, an increase in IRD flux during this interval also occurs in core GVY001, which has no evidence of turbidite deposition. At GVY001, the IRD flux during H3 is eight times higher than in V28-82. A comparison of IRD concentration and mass flux, two variables used to calculate IRD flux, reveals that much of the difference in IRD flux between V28-82 and the two western cores comes from the difference in mass flux. This comparison confirms that while IRD was an important sedimentary component at all three core locations, much more of it was deposited in the west than the east (Figure 4 a and b).

Since the eastern core displays much lower IRD flux during H3 and H6, a stronger zonal flux gradient may have existed during these two periods – more icebergs melted in the western basin, with fewer icebergs reaching and depositing IRD in the eastern region. The distinct melting patterns could be explained by any one, or a combination of, the following three factors: The calving flux from the Laurentide may have been smaller in magnitude during H3 and H6 so the majority of the drifting ice melted in the western NA without making it to the east; some different ice sheet(s) may have contributed to or dominated calving during this interval; or the surface ocean current patterns were different, causing changed iceberg trajectories.

If the calving of icebergs from the Laurentide ice sheet increased during H3 and H6, but to a lesser extent than during the other events, the IRD fluxes associated with these two events would display a visible but smaller increase than in the typical HEs across the subpolar Atlantic and a possible gradient from west to east. At face value, our data are consistent with this hypothesis. H3 and H6 do display increases in IRD flux that are smaller in magnitude than the other events, and there is a clear depositional gradient. Several hypotheses have been proposed to explain the smaller magnitude of calving during these events. Gwiazda et al. (1996) speculated that the ice sheet volume during H3 and H6 could have been smaller, leading to the smaller magnitude of calving. The logic of Gwiazda et al. is based on the observation that H3 and H6 occurred at the onset of the MIS 2 and 4, when the Laurentide ice sheet was just starting to regrow after periods of interglacial warmth. A similar yet distinct hypothesis states that H4, which in our western cores appears to be a particularly large event, “gutted” the Hudson Strait, removing it of all ice (Kirby and Andrews, 1999). As a result, H3 occurred when the Laurentide was still in a growth phase. The lack of a signal of H3 and H6 in V28-82 to the east might also reflect the greater distance from the source of icebergs, or the possibility that H3 and H6 icebergs were less dirty (Andrews, 2000; Kirby and Andrews, 1999). However, we are not aware of any evidence to suggest that H3 and H6 icebergs were particularly clean compared to icebergs in other HEs.

It has also been suggested that H3 and H6 may have had a European ice sheet origin (Grousset et al., 2000, 1993; Snoeckx et al., 1999). Our data do not support an entirely European origin for H3 and H6, since the deposition of IRD during each was demonstrably greater in the western North Atlantic. An iceberg trajectory model supports the unlikeliness of this scenario and suggests that the icebergs originating from the European ice sheet are mostly confined to the Norwegian Sea (Death et al., 2006). However, we cannot rule out that associated or precursor events of a European origin took place.

Our data do not directly support the hypothesis that warmer SST or a reorganization of the circulation pattern led to more iceberg melting in the west during H3 and H6. Although IRD fluxes increased during H3 and H6 at our western sites, the fluxes are not higher than during the other HEs. Combined with the essential lack of increased IRD deposition at the eastern site, the total IRD flux during H3 and H6 appears to be lower compared to the other events.

IRD flux reconstruction provides a potentially important constraint on modeled iceberg discharge during HEs as a freshwater delivery mechanism (Death et al., 2006). While most HE modeling studies have focused on meltwater (Ganopolski and Rahmstorf, 2001; Prange et al., 2004; Roberts et al., 2014) and iceberg calving (Alvarez-Solas et al., 2013, 2010; Bassis et al., 2017; Marshall and Koutnik, 2006), the absolute fluxes of meltwater and iceberg calving are challenging to reconstruct with paleo proxies. Meltwater proxies, including $\delta^{18}O$ (Cortijo et al., 1997; Roche et al., 2004), %C37:4 (Naafs et al., 2011; Rodrigues et al., 2017; Stein et al., 2009), and $^{10}Be/^{9}Be$ (Valletta et al., 2018), while valuable, are currently only qualitative. IRD grain concentration can only provide a relative measure of the magnitude of iceberg calving (e.g., Bond et al., 1992). In contrast, IRD flux is a proxy that is both quantitative and accessible, with the potential for comparable model output. A better understanding of the IRD entrainment and delivery mechanisms could be developed by incorporating IRD fluxes into ice sheet calving simulations. The direct data-model comparison of IRD flux can potentially help assess ice sheet calving simulations and improve the understanding of calving behaviors.

5.2. Sea surface proxies

The relative abundance of polar foraminifera (% *N. pachy.*) at GVY001 is saturated at 100% for most of the last glacial period, possibly due to the site's more poleward location (Figure 3). The % *N. pachy.* data from JPC37 exhibit more variability, with increases in every HE layer, indicating repeated sea-surface cooling. During H1, H2, and H4, % *N. pachy*. seems to show a double peak structure. The double peak might suggest that the SST is lowest at the beginning and end of these

HEs but briefly returned to warmer temperatures midway through the events. We do not see a similar sequence of delayed onset in the deposition of IRD after the initial increase in *N. pachy.* abundance, as reported previously (Barker et al., 2015).

The $\delta^{18}O$ of *N. pachy*. from JPC37 displays both the typical sawtooth glacial-interglacial cycle and episodes of depletion associated with HEs (Figure 3h). Given the % *N. pachy*. increase and therefore implied SST decrease during HEs, the depletion of $\delta^{18}O$ cannot be the result of temperature changes. The likely explanation is that the melting icebergs released a large amount of $\delta^{18}O$-depleted freshwater during each HE. A depletion of planktic $\delta^{18}O$ is not obvious in H6 and HQ (discussed in the next section), but neither did it become enriched during these periods. In light of the concurrent % *N. pachy*. increases, we suggest that just as during the other HEs, an influx of freshwater reached this site during H6 and HQ. The depletion of *N. pachy.* $\delta^{18}O$ is consistent with previous studies on North Atlantic cores (Bond et al., 1992; Cortijo et al., 1997; Hillaire-Marcel et al., 1994; Labeyrie et al., 1999). Cortijo et al. (1997) mapped out changes in *N. pachy.* $\delta^{18}O$ across the North Atlantic during H4. The magnitude of changes observed in JPC37 during H4 (~1 ‰) is comparable to a nearby core from that study (1.1 ‰ at SU90-11).

A cross-correlation of *N. pachy.* $\delta^{18}O$ and $^{230}Th_{xs}$ from JPC37 during the period between H1-6 shows little lag between the two variables (Figure S5). This simultaneity is robust on a range of interpolation intervals and does not change when the starting and ending times are varied by a few thousand years. The deposition of debris and local freshening of the sea surface were thus contemporaneous events on the time scale resolvable by our record. That is consistent with both phenomena being the direct consequence of melting icebergs, although we cannot rule out the accompanying presence of additional meltwater.

5.3. Extra events

Although H1-6 are the most commonly known and studied HEs of the last glacial period (e.g., Bond et al., 1992; Broecker et al., 1992; Grousset et al., 2000; Marcott et al., 2011), Heinrich (1988) postulated the existence of additional events in the early glacial and late interglacial period. A recent ice sheet modeling study (Bassis et al., 2017) predicted a previously unidentified HE that they named HQ at ~65 ka. Our IRD flux from JPC37 provides the strongest evidence yet of the existence of HQ.

The basis of our age model is partially the alignment of millennial-scale cooling events (C16-C24) identified throughout the North Atlantic region (McManus et al., 1994), including on the Iberian margin (Martrat et al., 2007; Greenland Stadial (GS) 17-25). Bassis et al. predicted the occurrence of HQ during GS19, or C18 in the framework of the cooling events. There are two distinct IRD-flux events within C16 and C18. If the younger event is H6, consistent with an age of ~60 ka (Bassis et al., 2017; Bond et al., 1999; Hemming 2004; Martrat et al., 2007), it thus seems likely that the older event of the two is the hypothesized event HQ. Given that Bassis et al. identified H7b prior to HQ within C19, which we identified with our % *N. pachy*. record, it is unlikely that we mistake HQ for an earlier HE. These two IRD flux events also cannot be H5a (Rashid et al., 2003) since we found Ash Zone 2 at a shallower depth in the core. Ash Zone 2 is between H5a and H6, which gives us confidence with the designation of H6. The fact that HQ is potentially found in JPC37 but was absent in previous studies suggests that the influence of the event may be regionally limited, but it also raises the possibility that HQ and H6 may be mistaken for one another in previous studies. Therefore, we recommend that ocean sediment studies that seek to identify H6 or HQ should have an accompanying SST proxy to resolve cooling events C16 and C18.

During the late last interglacial period at 70, 78, 87, 105, 109, and 117 ka, we found six additional IRD flux increases in JPC37 (Figure S6). These IRD flux increases were two orders of magnitude smaller than HEs, and unlike the typical HEs, changes in Ca/Sr, magnetic susceptibility, density, % coarse, % IRD, and % *N. pachy.*, do not accompany the IRD flux increases or have a temporal offset with the IRD flux increases. Another difference, relative to the HEs, is that most of these interglacial IRD flux increases were preceded by discernable mass flux increases (Figure S7). This repeated sequence of events may give us a clue as to their origins. According to the turbidite-IRD sequence previously proposed to explain IRD layers in the Labrador Sea (Rashid et al., 2012), the early high mass flux could be caused by the initial meltwater discharge and the ensuing turbidity and nepheloid flow. This mechanism would increase mass flux without bringing in IRD. Following the turbidite facies, IRD would have been deposited as icebergs were discharged. The number of these locally high IRD flux events we identified corresponds to the number of cooling events during the last interglacial period proposed by McManus et al. (1994), which we tentatively marked in Figure S6 and S7.

The lack of associated signals in other typical HE proxies (Figure S6 and S7) during most of these cooling events raises questions about their nature. Among other explanations, the magnitude of the events could have been too small to have detectable changes in typical HE proxies. Alternatively, the source region of the delivered materials may have changed, which could have led to the muted responses in Ca/Sr and magnetic susceptibility. These events could also have been the result of meltwater outbursts, similar to the 8.2 ka event (Alley et al., 1997; Ellison et al., 2006; Keigwin et al., 2005). A fourth potential explanation is that they were triggered by deep turbidity currents, as suggested by Hillaire-Marcel et al. (1994). Given that most of the events were associated with increases in % *N. pachy*., it is unlikely that they were caused by the deep turbidity currents alone, although a combination of the above mechanisms is still possible.

6. Conclusions

(1) The IRD flux in the western North Atlantic cores JPC37 and GVY001 increased during each HE during the last glacial cycle. A single mechanism may therefore account for all HE during this period.

(2) Compared to the only other available $^{230}Th_{xs}$-based IRD flux record, which is in the eastern North Atlantic, the western sites experienced much higher IRD flux during all HEs, notably including H3 and H6. We suggest that these two events, in the western North Atlantic at least, were the result of increased ice calving, rather than solely the result of other mechanisms such as increased foraminifera dissolution or reduced productivity.

(3) IRD fluxes during H3 and H6 in the western North Atlantic are smaller than the other typical HEs. This result is most consistent with the hypothesis that the calving of icebergs from the LIS increased during H3 and H6 but to a lesser extent than during the other events.

(4) All HEs were accompanied by surface cooling and freshening in the western subpolar North Atlantic.

(5) A series of previously identified cooling events during the MIS 5 interglacial were found in JPC37, accompanied by evidence for increased ice rafting that was two orders of magnitude smaller than HEs. These findings confirm the regional extent and limited impact of these stadial events.

Acknowledgements

The authors thank Martin Fleisher for assistance with U-Th procedure and ICP-MS analysis. We thank the crew of the RRS Discovery, chief scientist Kate Hendry, Laura Robinson, and members of the ICY-LAB team for acquiring GVY001. We are grateful to the staff of the BOSCORF for their support and the use of their equipment. We thank Grace Cushman for help with core archiving and sample processing. This research was funded by NSF grant AGS 16-35019 to JFM.

Appendix A. Supplementary material

All data are archived in PANGAEA and will be made public upon publication. Reviewers can temporarily access them with this link: https://www.pangaea.de/tok/f2915574eee9270de2552d634d19422d0680d4da

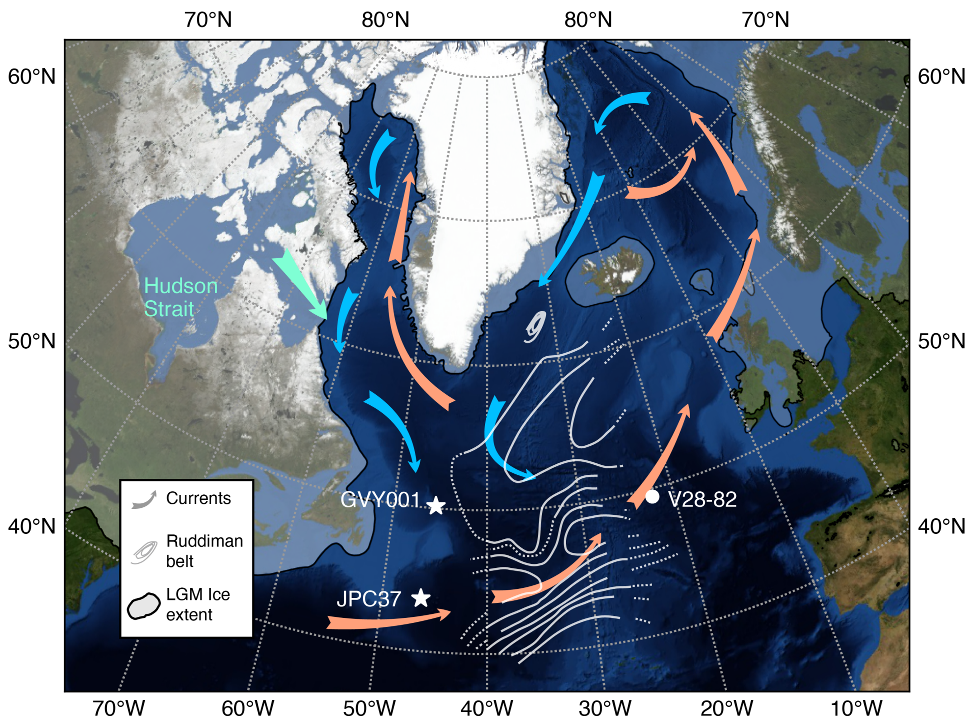

Figure 1. North Atlantic map with core locations. Stars depict the locations of cores used by this study: JPC37 (43°58'N, 46°25'W, 3981 m); GVY001 (50°09'36''N, 45°30'36''W, 3721 m). The white dot is the core used for comparison of IRD flux: V28-82 (49°27'N, 22°16'W, 3935 m) (McManus et al., 1998). The frosted area represents ice sheet extent during the Last Glacial Maximum (Ehlers et al., 2011). Red and blue arrows are the warm and cold surface circulation, respectively, after (Hemming et al., 2002). Aqua arrow leaving the Hudson Strait represents the calving of icebergs from the LIS. Contours delineate the Ruddiman IRD belt (Ruddiman, 1977). Basemap from NASA Blue Marble June image (Stockli et al., 2005).

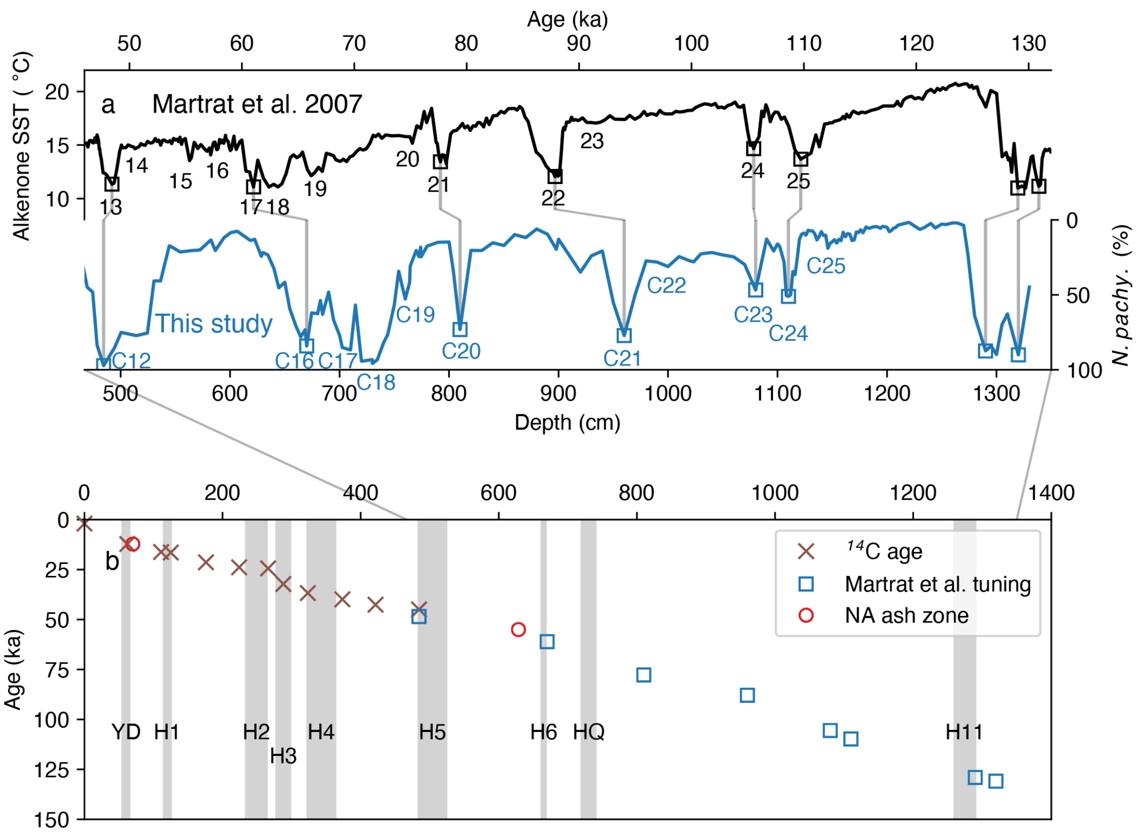

Figure 2. Chronology of JPC37. Variations in *N. pachy.* relative abundance are correlated with an alkenone unsaturation SST record (Martrat et al., 2007; Iberian margin stadials marked in black numbers) (a). That SST record was previously tied to the North Greenland Ice Core Project (NGRIP) chronology. Blue numbers denote cooling events (McManus et al., 2002, 1994, see Figure S8 for details). Tie points to our core are marked by thin gray lines. The lower panel contains the compilation of all age control points, including radiocarbon dating, tephrochronology, and tuning with alkenone record (b).

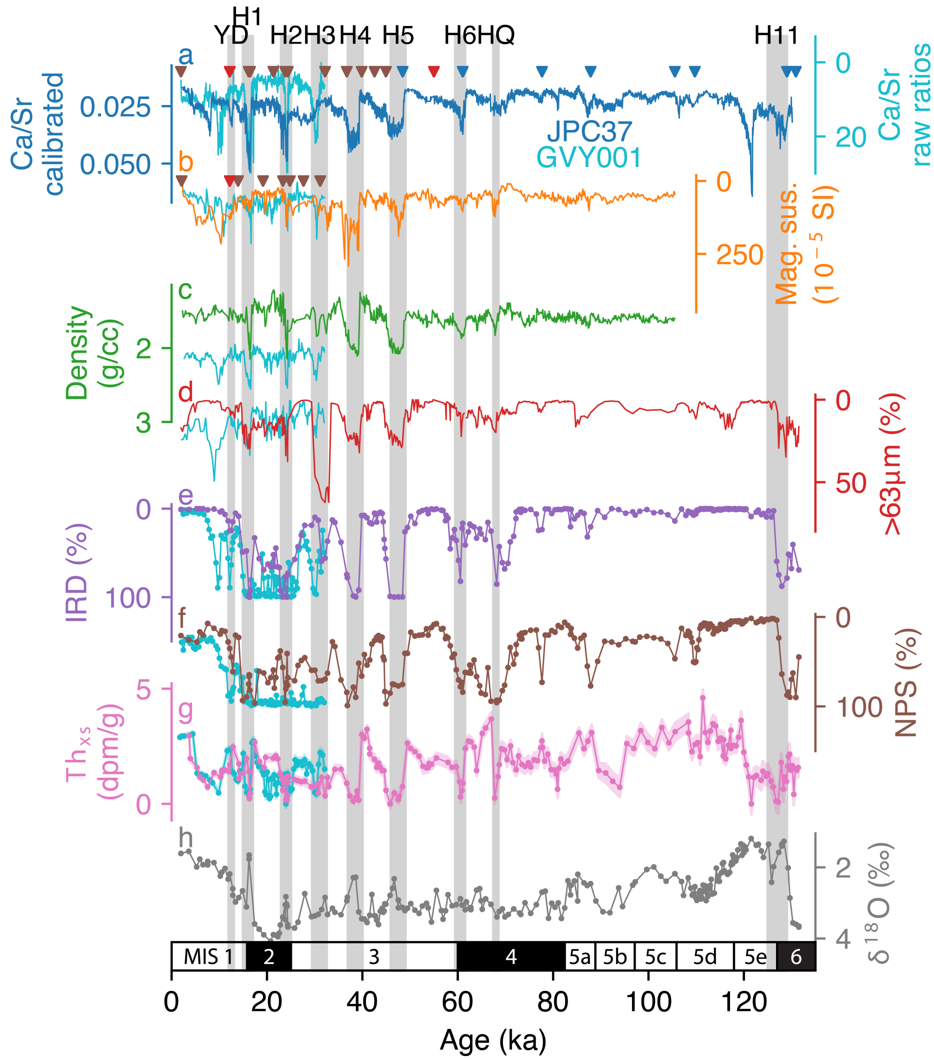

485
486 **Figure 3.** GVY001 (cyan) and JPC37 (other colors) Ca/Sr with JPC37 age control points marked by red
487 (ash zone), brown (radiocarbon), and blue (SST tie points) triangles (a), magnetic susceptibility with
488 GVY001 age control point marked by red (ash zone) and brown (radiocarbon) triangles (b), bulk wet
489 sediment density (c), coarse (>63μm) fraction (d), IRD abundance (e), *N. pachy.* abundance, of which the
490 early last interglacial (95-125 ka) data are partially from McManus et al. (2002) (f), $^{230}Th_{xs}$ with shading
491 marking 2σ uncertainty (g), and *N. pachy.* $\delta^{18}O$ (h). Gray bars are Younger Dryas (YD), H1-6, H11, as
492 well as HQ, as predicted by Bassis et al. (2017).
493

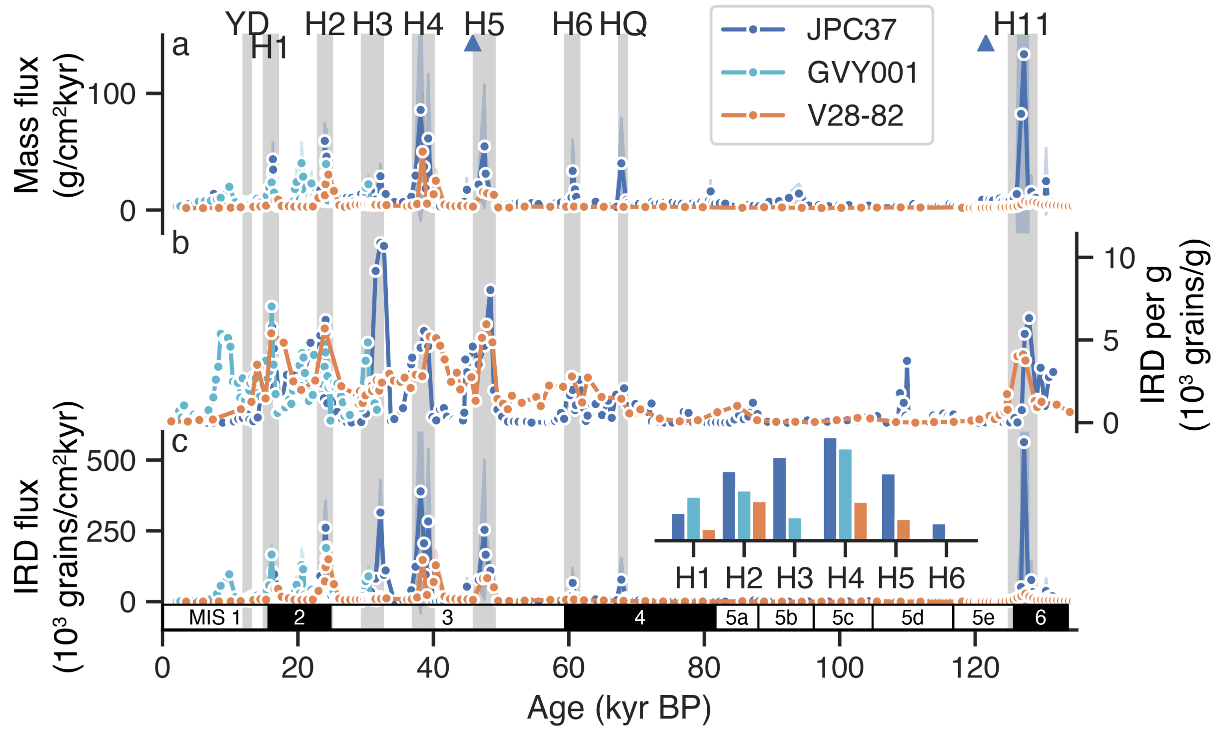

Figure 4. Comparison of JPC37, GVY001, and V28-82 $^{230}Th_{xs}$-normalized mass flux (a), IRD concentration (b), and IRD flux (c). Triangles in (a) are mass flux data points too high to quantify. The bar plot inset in (c) compares maximum IRD flux during each HE relatively. Although the Y-axis for the inset is omitted for simplicity, the bar heights are drawn proportionally.

Study	**($^{238}U/^{232}Th)_{detrital}$** used
Veiga-Pires and Hillaire-Marcel, 1999	**0.58**
Thomson et al., 1995	**0.67**
Thomson et al., 1999	**0.7**
McManus et al., 2004	**0.57**
Henderson and Anderson, 2003	**0.6**
Böhm et al., 2015	**0.47**
Bourne et al., 2012	**0.55**
Gherardi et al., 2009	**0.6**
Lippold et al., 2009	**0.5**
Lippold et al., 2011	**0.5**

Lippold et al., 2016	**0.6**
Guihou et al., 2010	**0.5**
Guihou et al., 2011	**0.5**
Roberts et al., 2014	**0.6**

Table 1. *Detrital U/Th used by previous studies. The range of the values is 0.47 – 0.7.*

References

Alley, R.B., Mayewski, P.A., Sowers, T., Stuiver, M., Taylor, K.C., Clark, P.U., 1997. Holocene climatic instability: A prominent, widespread event 8200 yr ago. Geology 25, 483–486.

Alvarez-Solas, J., Charbit, S., Ritz, C., Paillard, D., Ramstein, G., Dumas, C., 2010. Links between ocean temperature and iceberg discharge during Heinrich events. Nature Geoscience 3, 122–126. https://doi.org/10.1038/ngeo752

Alvarez-Solas, J., Robinson, A., Montoya, M., Ritz, C., 2013. Iceberg discharges of the last glacial period driven by oceanic circulation changes. Proceedings of the National Academy of Sciences 110, 16350–16354. https://doi.org/10.1073/pnas.1306622110

Andersen, M.B., Stirling, C.H., Zimmermann, B., Halliday, A.N., 2010. Precise determination of the open ocean $^{234}U/^{238}U$ composition. Geochemistry, Geophysics, Geosystems 11. https://doi.org/10.1029/2010GC003318

Anderson, R.F., Fleisher, M.Q., Lao, Y., 2006. Glacial-interglacial variability in the delivery of dust to the central equatorial Pacific Ocean. Earth and Planetary Science Letters 242, 406–414. https://doi.org/10.1016/j.epsl.2005.11.061

Andrews, J.T., 2000. Icebergs and Iceberg Rafted Detritus (IRD) in the North Atlantic: Facts and Assumptions. Oceanography 13, 100–108. https://doi.org/10.5670/oceanog.2000.19

Andrews, J.T., Voelker, A.H.L., 2018. “Heinrich events” (& sediments): A history of terminology and recommendations for future usage. Quaternary Science Reviews 187, 31–40. https://doi.org/10.1016/j.quascirev.2018.03.017

Ausín, B., Haghipour, N., Wacker, L., Voelker, A. H. L., Hodell, D., Magill, C., Looser, N., Bernasconi, S. M., Eglinton, T. I., 2019. Radiocarbon age offsets between two surface dwelling planktonic foraminifera species during abrupt climate events in the SW Iberian margin. Paleoceanography and Paleoclimatology, 34, 63–78. https://doi.org/10.1029/2018PA003490

Bacon, M.P., 1984. Glacial to interglacial changes in carbonate and clay sedimentation in the Atlantic Ocean estimated from ^{230}Th measurements. Chemical Geology 46, 97–111. https://doi.org/10.1016/0009-2541(84)90183-9

Bacon, M.P., Anderson, R.F., 1982. Distribution of thorium isotopes between dissolved and particulate forms in the deep sea. Journal of Geophysical Research 87, 2045. https://doi.org/10.1029/JC087iC03p02045

Bacon, M.P., Rosholt, J.N., 1982. Accumulation rates of Th-230, Pa-231, and some transition metals on the Bermuda Rise. Geochimica et Cosmochimica Acta 46, 651–666. https://doi.org/10.1016/0016-7037(82)90166-1

Bard, E., Rostek, F., Turon, J.L., Gendreau, S., 2000. Hydrological impact of Heinrich events in the subtropical Northeast Atlantic. Science 289, 1321–1324. https://doi.org/10.1126/science.289.5483.1321

Barker, S., Chen, J., Gong, X., Jonkers, L., Knorr, G., Thornalley, D., 2015. Icebergs not the trigger for North Atlantic cold events. Nature 520, 333–336. https://doi.org/10.1038/nature14330

Barker, S., Diz, P., Vautravers, M.J., Pike, J., Knorr, G., Hall, I.R., Broecker, W.S., 2009. Interhemispheric Atlantic seesaw response during the last deglaciation. Nature 457, 1097–1102. https://doi.org/10.1038/nature07770

Barnes, C.E., Cochran, J.K., 1990. Uranium removal in oceanic sediments and the oceanic U balance. Earth and Planetary Science Letters 97, 94–101. https://doi.org/10.1016/0012-821X(90)90101-3

Bassis, J.N., Petersen, S. V., Mac Cathles, L., 2017. Heinrich events triggered by ocean forcing and modulated by isostatic adjustment. Nature 542, 332–334. https://doi.org/10.1038/nature21069

Bond, G., Heinrich, H., Broecker, W., Labeyrie, L., McManus, J., Andrews, J., Huon, S., Jantschik, R., Clasen, S., Simet, C., Tedesco, K., Klas, M., Bonani, G., Ivy, S., 1992. Evidence for massive discharges of icebergs into the North Atlantic ocean during the last glacial period. Nature 360, 245–249. https://doi.org/10.1038/360245a0

Bond, G.C., Broecker, W.S., Johnsen, S.J., McManus, J.F., Labeyrie, L., Jouzel, J., Bonani, G., 1993. Correlation Between Climate Records From North Atlantic Sediments and Greenland Ice. Nature 365, 143–147.

Bourne, M.D., Thomas, A.L., Niocaill, C. Mac, Henderson, G.M., 2012. Improved determination of marine sedimentation rates using $^{230}Th_{xs}$. Geochemistry, Geophysics, Geosystems 13, 1–9. https://doi.org/10.1029/2012GC004295

Broecker, W.S., Andree, M., Bonani, G., Wolfli, W., Klas, M., Mix, A., Oeschger, H., 1988. Comparison between radiocarbon ages obtained on coexisting planktonic foraminifera. Paleoceanography 3, 647–657. https://doi.org/10.1029/PA003i006p00647

Broecker, W., Bond, G., Klas, M., Clark, E., McManus, J., 1992. Origin of the northern Atlantic's Heinrich events. Climate Dynamics 6, 265–273. https://doi.org/10.1007/BF00193540

Buizert, C., Sigl, M., Severi, M., Markle, B.R., Wettstein, J.J., McConnell, J.R., Pedro, J.B., Sodemann, H., Goto-Azuma, K., Kawamura, K., Fujita, S., Motoyama, H., Hirabayashi, M., Uemura, R., Stenni, B., Parrenin, F., He, F., Fudge, T.J., Steig, E.J., 2018. Abrupt ice-age shifts in southern westerly winds and Antarctic climate forced from the north. Nature 563, 681–685. https://doi.org/10.1038/s41586-018-0727-5

Cortijo, E., Labeyrie, L., Vidal, L., Vautravers, M., Chapman, M., Duplessy, J.-C., Elliot, M., Arnold, M., Turon, J.-L., Auffret, G., 1997. Changes in sea surface hydrology associated with Heinrich event 4 in the North Atlantic Ocean between 40° and 60°N. Earth and Planetary Science Letters 146, 29–45. https://doi.org/10.1016/S0012-821X(96)00217-8

Costa, K., McManus, J., 2017. Efficacy of ^{230}Th normalization in sediments from the Juan de Fuca Ridge, northeast Pacific Ocean. Geochimica et Cosmochimica Acta 197, 215–225. https://doi.org/10.1016/j.gca.2016.10.034

Costa, K.M., McManus, J.F., Anderson, R.F., 2017. Radiocarbon and Stable Isotope Evidence for Changes in Sediment Mixing in the North Pacific Over the Past 30 kyr. Radiocarbon 60, 1–23. https://doi.org/10.1017/RDC.2017.91

Costa, K.M., Hayes, C.M., Anderson, R.F., Pavia, F.J., Bausch, A., Deng, F., Dutay, J.-C., Geibert, W., Heinze, C., Henderson, G., Hillaire-Marcel, C., Hoffmann, S., Jaccard, S.L., Jacobel, A.W., Kienast, S.S., Kipp, L., Lerner, P., Lippold, J., Lund, D., Marcantonio, F., McGee, D., McManus, J.F., Mekik, F., Middleton, J.L., Missiaen, L., Not, C., Pichat, S., Robinson, L.F., Rowland, G.H., Roy-Barman, M., Tagliabue, A., Torfstein, A., Winckler, G., Zhou, Y. 230Th normalization: New insights on an essential tool for quantifying sedimentary fluxes in the modern and Quaternary ocean. Paleoceanography and Paleoclimatology 35, e2019PA003820. https://doi/org/10.1029/2019PA003820

Dansgaard, W., Johnsen, S.J., Clausen, H.B., Dahl-Jensen, D., Gundestrup, N.S., Hammer, C.U., Hvidberg, C.S., Steffensen, J.P., Sveinbjörnsdóttir, A.E., Jouzel, J., Bond, G.C., Sveinbjörnsdottir, A.E., Jouzel, J., Bond, G.C., 1993. Evidence for general instability of past climate from a 250-kyr ice-core record. Nature 364, 218–220. https://doi.org/10.1038/364218a0

Death, R., Siegert, M.J., Bigg, G.R., Wadley, M.R., 2006. Modelling iceberg trajectories, sedimentation rates and meltwater input to the ocean from the Eurasian Ice Sheet at the Last Glacial Maximum. Palaeogeography, Palaeoclimatology, Palaeoecology 236, 135–150. https://doi.org/10.1016/j.palaeo.2005.11.040

Ehlers, J., Ehlers, Jürgen, Gibbard, P.L., Hughes, P.D., 2011. Quaternary Glaciations - Extent and Chronology: A Closer Look. Elsevier.

Ellison, C.R.W., Chapman, M.R., Hall, I.R., 2006. Surface and Deep Ocean Interactions During the Cold Climate Event 8200 Years Ago. Science 312, 1929–1932. https://doi.org/10.1126/science.1127213

EPICA Community Members, 2004. Eight glacial cycles from an Antarctic ice core. Nature 429, 623–628. http://dx.doi.org/10.1038/nature02599

Ericson, D.B.., 1959. Coiling Direction of Globigerina pachyderma as a Climatic Index. Science 130, 219–220.

Fleisher, M.Q., Anderson, R.F., 1991. Particulate matter digestion (From Mg to 10's Of G) and radionuclide blanks. Geophysical Monograph Series 63, 221–222.

Francois, R., Bacon, M.P., Suman, D.O., 1990. Thorium 230 profiling in deep-sea sediments: high-resolution records of flux and dissolution of carbonate in the equatorial Atlantic during the last 24,000 years. Paleoceanography 5, 761–787. https://doi.org/0883-8305/90/90PA-016

Francois, R., Frank, M., Rutgers van der Loeff, M.M., Bacon, M.P., 2004. ^{230}Th normalization: An essential tool for interpreting sedimentary fluxes during the late Quaternary. Paleoceanography 19, PA1018. https://doi.org/10.1029/2003PA000939

Ganopolski, A., Rahmstorf, S., 2001. Rapid changes of glacial climate simulated in a coupled climate model. Nature 409, 153–158. https://doi.org/10.1038/35051500

Grootes, P.M., Stuiver, M., White, J.W.C., Johnsen, S., Jouzel, J., 1993. Comparison of oxygen isotope records from the GISP2 and GRIP Greenland ice cores. Nature 366, 552.

Grousset, F.E., Labeyrie, L., Sinko, J.A., Bond, G., Duprat, J., Cortijo, E., Cremer, M., Bond, G., Duprat, J., Cortijo, E., Huon, S., 1993. Patterns of Ice-Rafted Detritus in the Glacial North Atlantic (40-55°N). Paleoceanography 8, 175–192. https://doi.org/10.1029/92PA02923

Grousset, F.E., Pujol, C., Labeyrie, L., Auffret, G., A. Boelaert, A., 2000. Were the North Atlantic Heinrich events triggered by the behaviour of the European ice sheets? Geology 28, 123–126. https://doi.org/10.1130/0091-7613(2000)28<123:WTNAHE>2.0.CO;2

Gwiazda, R.H., Hemming, S.R., Broecker, W.S., 1996. Provenance of icebergs during Heinrich Event 3 and the contrast to their sources during other Heinrich episodes. Paleoceanography 11, 371–378. https://doi.org/10.1029/96PA01022

Heinrich, H., 1988. Origin and consequences of cyclic ice rafting in the Northeast Atlantic Ocean during the past 130,000 years. Quaternary Research 29, 142–152. https://doi.org/10.1016/0033-5894(88)90057-9

Hemming, S.R., 2004. Heinrich events: Massive late Pleistocene detritus layers of the North Atlantic and their global climate imprint. Reviews of Geophysics 42, 1–43. https://doi.org/10.1029/2003RG000128.1.INTRODUCTION

Hemming, S.R., Hall, C.M., Biscaye, P.E., Higgins, S.M., Bond, G.C., McManus, J.F., Barber, D.C., Andrews, J.T., Broecker, W.S., 2002. $^{40}Ar/^{39}Ar$ ages and $^{40}Ar^{*}$ concentrations of fine-grained sediment fractions from North Atlantic Heinrich layers. Chemical Geology 182, 583–603. https://doi.org/10.1016/S0009-2541(01)00342-4

Hendry, K.R., Huvenne, V.A., Robinson, L.F., Annett, A., Badger, M., Jacobel, A.W., Ng, H.C., Opher, J., Pickering, R.A., Taylor, M.L. and Bates, S.L., 2019. The biogeochemical impact of glacial meltwater from Southwest Greenland. Progress in Oceanography, 176, 102126. https://doi.org/10.1016/j.pocean.2019.102126

Henry, L.G., Mcmanus, J.F., Curry, W.B., Roberts, N.L., Piotrowski, A.M., Keigwin, L.D., 2016. North Atlantic ocean circulation and abrupt climate change during the last glaciation. Science 353, 470–474. https://doi.org/10.1126/science.aaf5529

Hillaire-Marcel, C., Vernal, A. de, Bilodeau, G., Wu, G., 1994. Isotope stratigraphy, sedimentation rates, deep circulation, and carbonate events in the Labrador Sea during the last ~200 ka. Can. J. Earth Sci. 31, 63–89. https://doi.org/10.1139/e94-007

Hodell, D.A., Channeil, J.E.T., Curtis, J.H., Romero, O.E., Röhl, U., 2008. Onset of "Hudson Strait" Heinrich events in the eastern North Atlantic at the end of the middle Pleistocene transition (~640 ka)? Paleoceanography 23, 1–16. https://doi.org/10.1029/2008PA001591

Johnsen, S.J., Clausen, H.B., Dansgaard, W., Fuhrer, K., Gundestrup, N.S., Hammer, C.U., Iversen, P., Jouzel, J., Stauffer, B., Steffensen, J.P., 1992. Irregular glacial interstadials recorded in a new Greenlan ice core. Nature 359, 311. https://doi.org/10.1038/350055a0

Johnsen, S.J., Dahl-Jensen, D., Gundestrup, N., Steffensen, J.P., Clausen, H.B., Miller, H., Masson-Delmotte, V., Sveinbjörnsdottir, A.E., White, J., 2001. Oxygen isotope and palaeotemperature records from six Greenland ice-core stations: Camp Century, Dye-3, GRIP, GISP2, Renland and NorthGRIP. Journal of Quaternary Science 16, 299–307. https://doi.org/10.1002/jqs.622

Jullien, E., Grousset, F.E., Hemming, S.R., Peck, V.L., Hall, I.R., Jeantet, C., Billy, I., 2006. Contrasting conditions preceding MIS3 and MIS2 Heinrich events. Global and Planetary Change 54, 225–238. https://doi.org/10.1016/j.gloplacha.2006.06.021

Keigwin, L.D., Sachs, J.P., Rosenthal, Y., Boyle, E.A., 2005. The 8200 year B.P. event in the slope water system, western subpolar North Atlantic. Paleoceanography 20. https://doi.org/10.1029/2004PA001074

Kirby, E., Andrews, T., 1999. Mid-Wisconsin Laurentide Ice Sheet growth and decay: Implications for Heinrich events 3 and 4. Paleoceanography 14, 211–223.

Klinkhammer, G.P., Palmer, M.R., 1991. Uranium in the oceans: Where it goes and why. Geochimica et Cosmochimica Acta 55, 1799–1806. https://doi.org/10.1016/0016-7037(91)90024-Y

Labeyrie, L., Leclaire, H., Waelbroeck, C., Cortijo, E., Duplessy, J.-C., Vidal, L., Elliot, M., Coat, B.L., Auffret, G., 1999. Temporal Variability of the Surface and Deep Waters of the North West Atlantic Ocean at Orbital and Millennial Scales, in: Mechanisms of Global Climate Change at Millennial Time Scales. American Geophysical Union (AGU), pp. 77–98. https://doi.org/10.1029/GM112p0077

Lao, Y., Anderson, R.F., Broecker, W.S., Hofmann, H.J., Wolfli, W., 1993. Particulate fluxes of ^{230}Th, ^{231}Pa, and ^{10}Be in the northeastern Pacific Ocean. Geochimica et Cosmochimica Acta 57, 205–217. https://doi.org/10.1016/0016-7037(93)90479-G

Manabe, S., Stouffer, R.J., 1997. Coupled ocean-atmosphere model response to freshwater input: Comparison to Younger Dryas Event. Paleoceanography 12, 321–336. https://doi.org/10.1029/96PA03932

Marcott, S.A., Clark, P.U., Padman, L., Klinkhammer, G.P., Springer, S.R., Liu, Z., Otto-Bliesner, B.L., Carlson, A.E., Ungerer, A., Padman, J., He, F., Cheng, J., Schmittner, A., 2011. Ice-shelf collapse from subsurface warming as a trigger for Heinrich events. Proceedings of the National Academy of Sciences 108, 13415–13419. https://doi.org/10.1073/pnas.1104772108

Marshall, S.J., Koutnik, M.R., 2006. Ice sheet action versus reaction: Distinguishing between Heinrich events and Dansgaard-Oeschger cycles in the North Atlantic. Paleoceanography 21, 1–13. https://doi.org/10.1029/2005PA001247

Martrat, B., Grimalt, J.O., Shackleton, N.J., de Abreu, L., Hutterli, M.A., Stocker, T.F., 2007. Four Climate Cycles of Recurring Deep and Surface Water Destabilizations on the Iberian Margin. Science 317, 502–507. https://doi.org/10.1126/science.1139994

McCartney, M., 1992. Recirculating components to the deep boundary current of the northern North Atlantic. Progress in Oceanography 29, 283–383.

McManus, J.F., Anderson, R.F., Broecker, W.S., Fleisher, M.Q., Higgins, S.M., 1998. Radiometrically determined sedimentary fluxes in the sub-polar North Atlantic during the last 140,000 years. Earth and Planetary Science Letters 155, 29–43. https://doi.org/10.1016/S0012-821X(97)00201-X

McManus, J.F., Bond, G.C., Broecker, W.S., Johnsen, S., Labeyrie, L., Higgins, S., 1994. High-resolution climate records from the North Atlantic during the last interglacial. Nature 371, 326–329. https://doi.org/10.1038/371326a0

McManus, J.F., Francois, R., Gherardi, J.-M., Keigwin, L.D., Brown-Leger, S., 2004. Collapse and rapid resumption of Atlantic meridional circulation linked to deglacial climate changes. Nature 428, 834–837. https://doi.org/10.1038/nature02494

McManus, J.F., Oppo, D.W., Keigwin, L.D., Cullen, J.L., Bond, G.C., 2002. Thermohaline Circulation and Prolonged Interglacial Warmth in the North Atlantic. Quaternary Research 58, 17–21. https://doi.org/10.1006/qres.2002.2367

Murray, R.W., Miller, D.J., Kryc, K.A., 2000. Analysis of major and trace elements in rocks, sediments, and interstitial waters by inductively coupled plasma-atomic emission spectrometry (ICP-AES). ODP Tech. Note.

Naafs, B.D.A., Hefter, J., Ferretti, P., Stein, R., Haug, G.H., 2011. Sea surface temperatures did not control the first occurrence of Hudson Strait Heinrich Events during MIS 16. Paleoceanography 26, 1–10. https://doi.org/10.1029/2011PA002135

NGRIP members, 2004. High-resolution record of Northern Hemisphere climate extending into the last interglacial period. Nature 431, 147–151. https://doi.org/10.1038/nature02805

Parrenin, F., Rémy, F., Ritz, C., Siegert, M.J., Jouzel, J., 2004. New modeling of the Vostok ice flow line and implication for the glaciological chronology of the Vostok ice core. Journal of Geophysical Research D: Atmospheres 109. https://doi.org/10.1029/2004JD004561

Peck, V.L., Hall, I.R., Zahn, R., Grousset, F., Hemming, S.R., Scourse, J.D., 2007. The relationship of Heinrich events and their European precursors over the past 60 ka BP: a multi-proxy ice-rafted debris provenance study in the North East Atlantic. Quaternary Science Reviews 26, 862–875. https://doi.org/10.1016/j.quascirev.2006.12.002

Prange, M., Lohmann, G., Romanova, V., Butzin, M., 2004. Modelling tempo-spatial signatures of Heinrich Events: influence of the climatic background state. Quaternary Science Reviews 23, 521–527. https://doi.org/10.1016/j.quascirev.2003.11.004

Rahmstorf, S., 1995. Bifurcations of the Atlantic thermohaline circulation in response to changes in the hydrological cycle. Nature 378, 145. https://doi.org/10.1038/378145a0

Rashid, H., Hesse, R., Piper, D.J.W., 2003. Evidence for an additional Heinrich event between H5 and H6 in the Labrador Sea. Paleoceanography 18, 1–15. https://doi.org/10.1029/2003PA000913

Rashid, H., Saint-Ange, F., Barber, D.C., Smith, M.E., Devalia, N., 2012. Fine scale sediment structure and geochemical signature between eastern and western North Atlantic during Heinrich events 1 and 2. Quaternary Science Reviews 46, 136–150. https://doi.org/10.1016/j.quascirev.2012.04.026

Rasmussen, S.O., Andersen, K.K., Svensson, A.M., Steffensen, J.P., Vinther, B.M., Clausen, H.B., Siggaard-Andersen, M.L., Johnsen, S.J., Larsen, L.B., Dahl-Jensen, D., Bigler, M., Röthlisberger, R., Fischer, H., Goto-Azuma, K., Hansson, M.E., Ruth, U., 2006. A new Greenland ice core chronology for the last glacial termination. Journal of Geophysical Research Atmospheres 111, 1–16. https://doi.org/10.1029/2005JD006079

Reimer, P.J., Edouard Bard, B., Alex Bayliss, B., Warren Beck, B.J., Paul Blackwell, B.G., Christopher Bronk Ramsey, B., 2013. Intcal13 and Marine13 Radiocarbon Age Calibration Curves 0–50,000 Years Cal Bp. Radiocarbon 55, 1869–1887. https://doi.org/10.2458/azu_js_rc.55.16947

Roberts, W.H.G., Valdes, P.J., Payne, A.J., 2014. A new constraint on the size of Heinrich Events from an iceberg/sediment model. Earth and Planetary Science Letters 386, 1-9, https://doi.org/10.1016/j.epsl.2013.10.020

Robinson, L.F., Noble, T.L., McManus, J.F., 2008. Measurement of adsorbed and total 232Th/230Th ratios from marine sediments. Chemical Geology 252, 169–179. https://doi.org/10.1016/j.chemgeo.2008.02.015

Roche, D., Paillard, D., Cortijo, E., 2004. Constraints on the duration and freshwater release of Heinrich event 4 through isotope modelling. Nature 432, 379–382. https://doi.org/10.1038/nature03059

Rodrigues, T., Alonso-García, M., Hodell, D.A., Rufino, M., Naughton, F., Grimalt, J.O., Voelker, A.H.L., Abrantes, F., 2017. A 1-Ma record of sea surface temperature and extreme cooling events in the North Atlantic: A perspective from the Iberian Margin. Quaternary Science Reviews 172, 118–130. https://doi.org/10.1016/j.quascirev.2017.07.004

Ruddiman, W.F., 1977. North Atlantic Ice-Rafting: A Major Change at 75,000 Years Before the Present. Science (New York, N.Y.) 196, 1208–1211. https://doi.org/10.1126/science.196.4295.1208

Ruddiman, W.F., Glover, L.K., 1972. Vertical mixing of Ice-rafted volcanic Ash in North Atlantic Sediments. Geological Society of America Bulletin 83, 2817–2836.

Snoeckx, H., Grousset, F., Revel, M., Boelaert, A., 1999. European contribution of ice-rafted sand to Heinrich layers H3 and H4. Marine Geology 158, 197–208. https://doi.org/10.1016/S0025-3227(98)00168-6

Southon, J., 2004. A Radiocarbon Perspective on Greenland Ice-Core Chronologies: Can we Use Ice Cores for 14C Calibration? Radiocarbon 46, 1239–1259. https://doi.org/10.1017/S0033822200033129

Stein, R., Hefter, J., Grützner, J., Voelker, A., David A Naafs, B., 2009. Variability of surface water characteristics and Heinrich-like events in the Pleistocene midlatitude North Atlantic Ocean: biomarker and XRD records from IODP site U1313 (MIS 16-9). Paleoceanography 24, 1–13. https://doi.org/10.1029/2008PA001639

Stockli, R., Vermote, E., Saleous, N., Simmon, R., Herring, D., 2005. The Blue Marble Next Generation - A true color earth dataset including seasonal dynamics from MODIS.

Stuiver, M., Reimer, P.J., Reimer, R.W., 2019. CALIB 7.1 [WWW program].

Svensson, A., Andersen, K.K., Bigler, M., Clausen, H.B., Dahl-Jensen, D., Davies, S.M., Johnsen, S.J., Muscheler, R., Parrenin, F., Rasmussen, S.O., Röthlisberger, R., Seierstad, I., Steffensen, J.P., Vinther, B.M., 2008. A 60 000 year Greenland stratigraphic ice core chronology. Climate of the Past 4, 47–57. https://doi.org/10.5194/cp-4-47-2008

Valletta, R.D., Willenbring, J.K., Passchier, S., Elmi, C., 2018. ^{10}Be/ ^{9}Be Ratios Reflect Antarctic Ice Sheet Freshwater Discharge During Pliocene Warming. Paleoceanography and Paleoclimatology. https://doi.org/10.1029/2017PA003283

Supporting Information for

Enhanced iceberg discharge in the western North Atlantic during all Heinrich events of the last glaciation

Yuxin Zhou[1,2], Jerry F. McManus[1,2], Allison W. Jacobel[3], Kassandra M. Costa[4], Shouyi Wang[4], Blanca Alvarez Caraveo[5]

[1]Lamont-Doherty Earth Observatory of Columbia University, Palisades, NY 10964, USA

[2]Dept. of Earth and Environmental Sciences, Columbia University, New York, NY 10027, USA

[3]Institute at Brown for Environment and Society, Providence, RI 02912, USA

[4]Dept. of Earth, Environmental, and Planetary Sciences, Brown University, Providence, RI 02912, USA

[5]Dept. of Geology and Geophysics, Woods Hole Oceanographic Institution, Woods Hole, MA 02543, USA

[6]Dept. of Atmospheric and Oceanic Sciences, University of California, Los Angeles, Los Angeles, CA 90095, USA

Contents of this file

Text S1

Figures S1 to S8

Additional Supporting Information (Files uploaded separately)

Tables S1 to S22 are uploaded to PANGAEA and can be temporarily accessed by reviewers with this link: https://www.pangaea.de/tok/f2915574eee9270de2552d634d19422d0680d4da

Introduction

The text presented here discusses the U-Th systematics, and the figures further characterize the physical and chemical properties of the two cores used by this study.

In Text S1, we discuss the choices made in calculating $^{230}Th_{xs}$, including the values of $(^{230}Th/^{238}U)_{detrital}$ and $(^{238}U/^{232}Th)_{detrital}$.

In Figure S1, we show the age model of GVY001.

In Figure S2, we show the core image of the turbidite sequence found at 280-290 cm depth in JPC37.

In Figure S3, we show the leaching experiment results from JPC37 for determining the detrital $^{230}Th/^{238}U$ ratio.

In Figure S4, we show the leaching experiment results from JPC37 for determining the detrital U/Th ratio.

In Figure S5, we show the phasing lag correlations of planktic $\delta^{18}O$ with $^{230}Th_{xs}$ from JPC37.

In Figure S6, the same as Figure 3, except we zoom in on the cooling events and the panel that displayed $^{230}Th_{xs}$ shows IRD flux instead.

In Figure S7, the same as Figure 4, except we zoom in on the cooling events.

In Figure S8, we show the last interglacial % *N. pachy.* from JPC37 and V29-191 side by side (McManus et al., 1994).

Text S1. The calculation of $^{230}Th_{xs}$ commonly assumes that the detrital decay chain of ^{238}U is in secular equilibrium ($^{238}U_{det} = {}^{230}Th_{det}$). This assumption is valid when an isotopic system is closed for a sufficient length of time. However, α recoil disrupts the closed system by potentially ejecting the decay product (^{234}U or ^{230}Th in this case) or leaving it within a damaged crystal lattice site. Recently, it has been suggested that 4% of the decayed ^{234}U is lost due to α recoil, and the decay of ^{234}U further ejects 4% of ^{230}Th (Bourne et al., 2012). These authors reasoned that the average value between 0.92 (1×0.96^2) and 1 (secular equilibrium), 0.96, should be used as the value of $(^{230}Th/^{238}U)_{detrital}$. Deep-sea sediments have also been observed within this range and somewhat lower (DePaolo et al., 2006). Our leaching experiment on sediments suggests that the effect of α recoil may be stronger than previously thought (Figure S3). The losses of ^{234}U and ^{230}Th are 10% each on average, although the uncertainty on ^{230}Th loss is greater than on ^{234}U. These data imply that, when calculating $^{230}Th_{xs}$, the detrital correction is smaller, leading to more ^{230}Th counted towards the scavenged portion. The result is a higher $^{230}Th_{xs}$. This correction, compared to the equilibrium assumption, increases $^{230}Th_{xs}$ during non-HE period by ~5%. Because the higher burial fluxes during HEs often result in very low $^{230}Th_{xs}$, the proportional change associated with this correction is even larger (up to 70%), although the absolute change is small.

A wide range of $(^{238}U/^{232}Th)_{detrital}$ has been used in the $^{230}Th_{xs}$ calculation in the North Atlantic, ranging from 0.47 to 0.7 (Table 1). These studies use either the $^{238}U/^{232}Th$ minimum measured, which is thought to reflect the minimal influence of authigenic ^{238}U, or a vaguely defined basin-wide value. More recently, it has been suggested that $(^{238}U/^{232}Th)_{detrital}$ may vary through time (Missiaen et al., 2018). Consistent with that study's conclusion, our leaching experiment from JPC37 (Figure S4) shows large variations in the detrital ratio. Since HE mass flux is the focus of this study, we choose to use the $(^{238}U/^{232}Th)_{detrital}$ that produces a conservative yet realistic estimate of mass flux throughout. The five leaching experiments made in Heinrich layer 4 provide a mean ratio of 0.48, which we use in this study. While this is toward the low end of the range of values previously applied for North Atlantic sediments, it is indeed within that range. Using higher ratios would yield negative $^{230}Th_{xs}$ in some cases, implying net sedimentary loss of ^{230}Th from settling particles to the water column, which we consider unlikely. The higher detrital ratios in other Heinrich layers could be due to the lower sampling resolution, which may not capture the lowest detrital ratios.

The relatively conservative but nonetheless very low $^{230}Th_{xs}$ results we obtained are useful to inform us that the subpolar western North Atlantic had episodically high fluxes of ice rafting. However, we are hindered in using $^{230}Th_{xs}$ to normalize the burial of $^{231}Pa_{xs}$. In other words, we cannot use Pa/Th as a tracer for circulation strength at this site. The low concentrations are overwhelmed by the magnitude of the combined, propagated uncertainties for Pa and Th, rendering our results so ambiguous that they are uninterpretable. Future studies aiming to use this approach to reconstruct rates of deep ocean circulation associated with iceberg discharges from the Laurentide should focus on sites further east or south to avoid being similarly overwhelmed by the increased IRD flux.

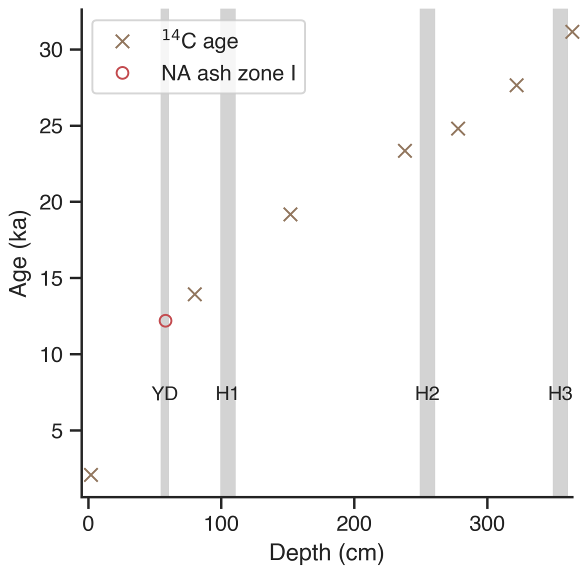

Figure S1. Chronology of GVY001.

Figure S2. Turbidite sequence found at 280-290 cm depth in JPC37, around the depth of Heinrich layer 3. The distance between the two core depth tags is 10 cm.

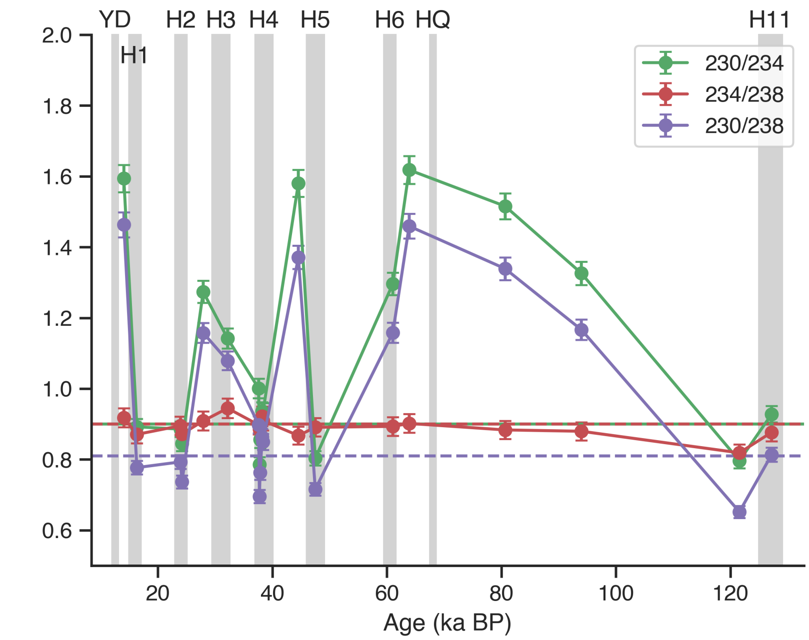

Figure S3. Leaching experiment results from JPC37 for determining the detrital $^{230}Th/^{238}U$ ratio. Dashed lines are the ratios used by this study (0.9 for $^{230}Th/^{234}U$ and $^{234}U/^{238}U$ and 0.81 for $^{230}Th/^{238}U$).

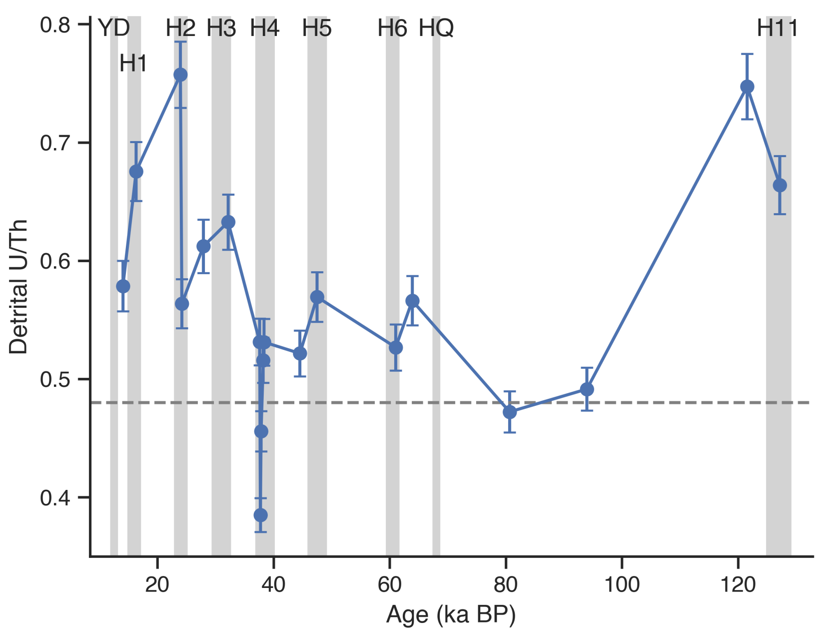

Figure S4. Leaching experiment results from JPC37 for determining the detrital U/Th ratio. The dashed line is the average ratio (0.48) of the high-resolution measurements within H4, which we use in $^{230}Th_{xs}$ normalization calculations in this study.

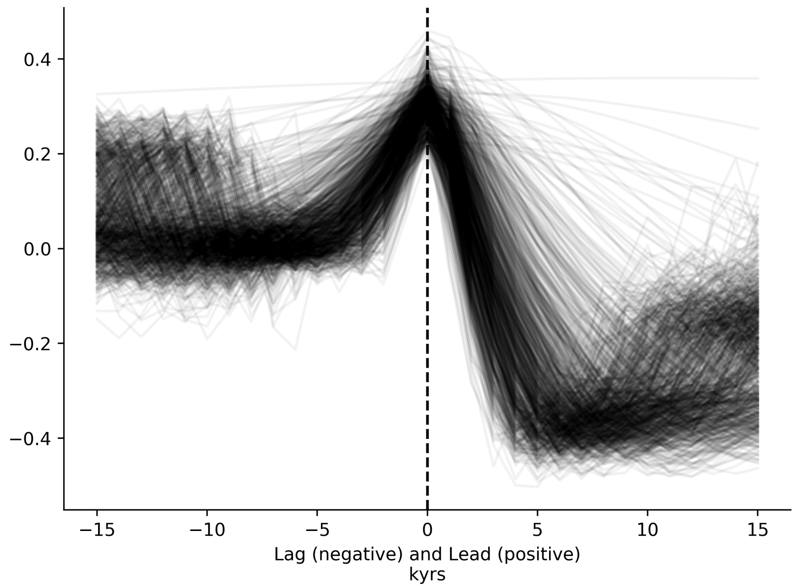

Figure S5. Phasing lag correlations of planktic $\delta^{18}O$ with $^{230}Th_{xs}$ from JPC37, bootstrapped 1000 times allowing sampling start time, end time, and time step to vary. The correlation coefficient in the positive (negative) direction is calculated when planktic $\delta^{18}O$ leads (lags) $^{230}Th_{xs}$.

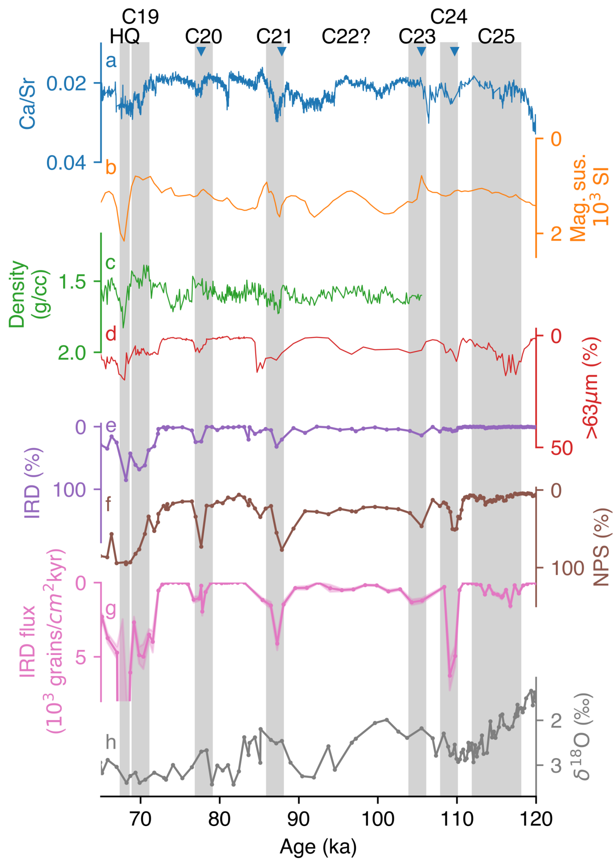

Figure S6. Same as Figure 3 except (g) displays IRD flux, limited to the late last interglacial period for the locally-high IRD flux events from JPC37, and assigned cooling events numbering according to McManus et al. (1994) and McManus et al. (2002). Shadings are HQ and cooling events.

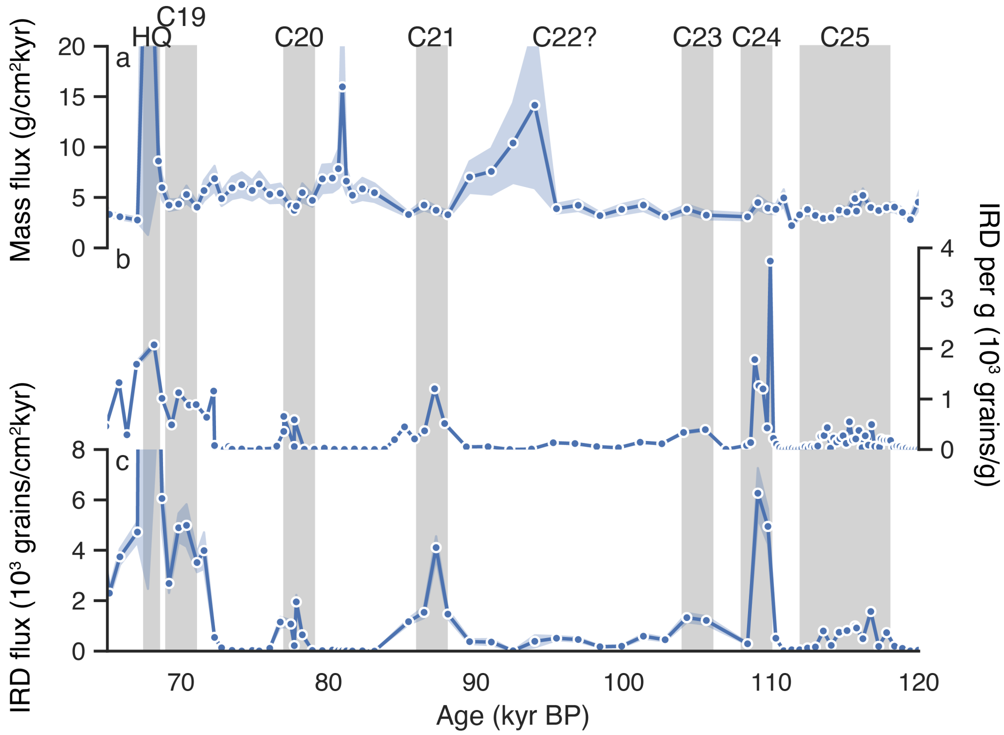

Figure S7. Same as Figure 4 but for the locally-high IRD flux events of the late last interglacial period from JPC37 and assigned cooling events tentatively according to McManus et al. (1994). Shadings are HQ and cooling events.

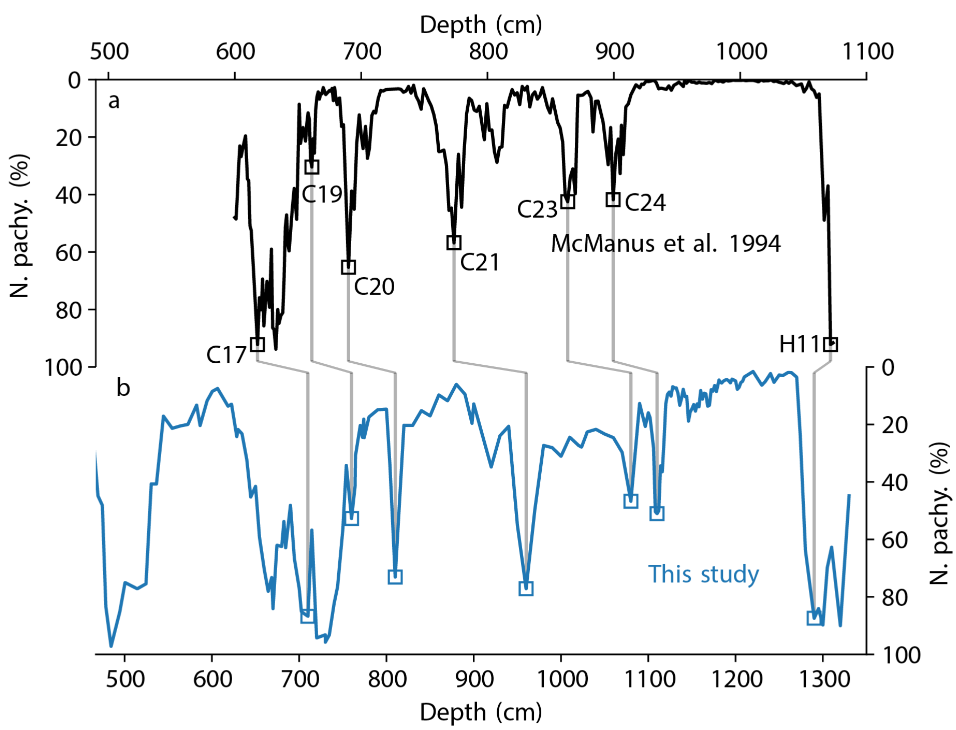

Figure S8. Correlation of last interglacial % *N. pachy.* between JPC37 and V29-191 (McManus et al., 1994).

References

Bourne, M.D., Thomas, A.L., Niocaill, C. Mac, Henderson, G.M., 2012. Improved determination of marine sedimentation rates using $^{230}Th_{xs}$. Geochemistry, Geophysics, Geosystems 13, 1–9. https://doi.org/10.1029/2012GC004295

DePaolo, D.J., Maher, K., Christensen, J.N., McManus, J., 2006. Sediment transport time measured with U-series isotopes: Results from ODP North Atlantic drift site 984. Earth and Planetary Science Letters 248, 379–395. https://doi.org/10.1016/j.epsl.2006.06.004

Missiaen, L., Pichat, S., Waelbroeck, C., Douville, E., Bordier, L., Dapoigny, A., Thil, F., Foliot, L., Wacker, L., 2018. Downcore Variations of Sedimentary Detrital ($^{238}U/^{232}Th$) Ratio: Implications on the Use of 230Thxs and 231Paxs to Reconstruct Sediment Flux and Ocean Circulation. Geochemistry, Geophysics, Geosystems 19, 2560–2573. https://doi.org/10.1029/2017GC007410